Nuclear Science and Techniques (2026) 37:87
https://doi.org/10.1007/s41365-026-01904-7

Reexamined mass of ^{22}C via the constraint from the recently experimental extraction of its radius

Yi-Le Fan[1] · Qing-Rui Sun[1] · Cheng-Jun Feng[1] · Yi-Bin Qian[1] · Dong Bai[2]

Received: 20 August 2025 / Revised: 30 September 2025 / Accepted: 4 November 2025 / Published online: 24 February 2026

Abstract
The neutron-rich nucleus ^{22}C, located at the neutron drip line, exhibits intriguing structural properties, such as its Borromean nature and potential two-neutron halo configuration. Despite experimental advancements, uncertainties persist in the two-neutron separation energy S_{2n} and the radius of matter for this attractive nucleus ^{22}C. In this study, we employed the three-body Faddeev approach to investigate the ground-state properties of ^{22}C, constrained by the recently deduced matter radius. By optimizing the neutron-core and three-body interactions to reproduce the experimental radius, the two-neutron separation energy S_{2n} was redetermined, revealing a weakly bound system dominated by the *s*-wave configuration. Additionally, an excited state exhibiting an Efimov-like pattern was identified by analyzing the specific density distributions and relative distances in the three-body system, highlighting the geometric similarity between the ground and excited states.

Keywords Two-neutron separation energy · Nuclear radius · Three-body approach · Neutron-rich nucleus

1 Introduction

With the advent of radioactive ion beam technology and facilities, the nuclear landscape has been extended to a large map, encompassing $Z = 118$ and reaching the proton and neutron drip line [1–3]. Contrary to the proton-rich side of the nuclear chart, experimental exploration of neutron-rich nuclei appears to be quite limited because of their short lifetimes and tiny cross sections [4–7]. Among these dripline nuclei, the heaviest carbon isotope is experimentally determined to be ^{22}C, which is of particular interest in both nuclear physics and Efimov physics in connection with its Borromean nature [8–11]. In detail, approximately two decades ago, ^{22}C was predicted to be an ideal *s*-wave two-neutron halo nucleus with a dominant $\nu(s_{1/2})^2$ configuration [12, 13], which was then confirmed in the measurement of the reaction cross section, regardless of the unexpectedly large matter radius [14]. In addition, this dripline nucleus ^{22}C plays a crucial role in other exotic structural properties, such as the possible new magicity at $N = 16$ and shape decoupling [15–20]. On the other hand, ^{22}C is, as mentioned before, a typical Borromean nucleus with a bound three-body (^{20}C+n+n) system, while no pair of its components, namely ^{20}C+n or n+n, is found. However, there are still large uncertainties and puzzles in its nuclear quantities, such as the separation energy and matter radius [2, 21–23].

In fact, since the astonishing experiment of the reaction of ^{22}C on a liquid hydrogen target in Ref. [14], extensive efforts have been made to clarify the ambiguity regarding the bulk properties of this intriguing nucleus [9, 21, 22]. For example, the interaction cross sections (σ_I) of ^{22}C on a carbon target were accurately measured at 235 MeV/nucleon, resulting in a σ_I of 1.280±0.023 b [9]. Within a four-body Glauber reaction model, the root-mean-squared matter radius of ^{22}C was deduced to be 3.44±0.08 fm, which is obviously smaller than the previous extraction. Several other experiments have also

This work was supported by the National Natural Science Foundation of China (Nos. 12075121 and 12375122), the Natural Science Foundation of Jiangsu Province (No. BK20190067), and the Fundamental Research Funds for the Central Universities (Nos. 30922010312 and B230201022).

✉ Yi-Bin Qian
qyibin@njust.edu.cn

1 Department of Applied Physics and MIIT Key Laboratory of Semiconductor Microstructure and Quantum Sensing, Nanjing University of Science and Technology, Nanjing 210094, China

2 College of Mechanics and Engineering Science, Hohai University, Nanjing 211100, China

been performed to understand the ^{22}C nuclear structure, such as neutron removal reactions from carbon isotopes and the reconstruction of ^{20}C+n decay-energy spectrum [8, 21, 22]. As another typical quantity for the dripline nuclei, the binding energy or the (two) neutron separation energy of ^{22}C is still uncertain. To date, there seems to be only one direct mass measurement of ^{22}C, leading to an upper limit of $S_{2n} \leq 320$ keV [23]. According to a recent atomic mass evaluation (AME 2020), the value of S_{2n} was determined to be 35±20 keV [2]. From a theoretical perspective, there are different choices for predicting separation energies within the shell model context and three-body approach [12, 24–26]. In addition, extensive efforts have been devoted to this exotic nucleus ^{22}C and its isotopes via the ab initio methods [27–29]. However, a debate or discussion seemingly exists regarding the knowledge of ^{22}C.

It is well expected and accepted that there is consistency between the neutron separation energy and matter radius for neutron-rich nuclei [12, 24, 30, 31]. In other words, such a correlation can allow us to at least place the constraint on the structural property of ^{22}C, although its absolute value of separation energy and matter radius may not be reached at present. Based on the extracted matter radii from the reaction measurements, the two-neutron separation energy of ^{22}C can be obtained via the empirical formula of the relationship between the energy and radius [23, 24, 32]. For example, under such a procedure, the S_{2n} of ^{22}C would be approximately 10 keV based on the large radius reported decades ago [24]. Recently, the reaction cross sections of neutron-rich carbon isotopes on ^{12}C were systematically measured over a wide range of incident energies from 30 to 950 MeV/nucleon [33]. The matter distributions and radii of the carbon isotopes are then determined by using the finite-range Glauber model with Coulomb correction, including the exotic nucleus ^{22}C. The simultaneously obtained charge radii were in excellent agreement with those directly extracted from the charge-change cross sections [33, 34]. Keeping these in mind, it is of particular significance to determine what one can obtain through the constraint of these new data with high accuracy. Against this background, the three-body Faddeev method is employed here to further understand the binding mechanism of ^{22}C via the two-neutron separation energy, with the condition of reproducing its matter radius. The details of the theoretical approach and the parameterization choice are presented in the next section, and the specific results and related discussions on the nucleon density distributions are provided in Sect. 3. Finally, a summary is presented in the last section.

2 Theoretical approach

The Faddeev equations provide a rigorous mathematical framework for three-body systems, whose essence lies in decomposing the total wave function into three Faddeev components (Ψ_1, Ψ_2, Ψ_3), each corresponding to and describing the pair-wise interaction between particles [35]. For instance, in the $^{22}\mathrm{C}\left(^{20}\mathrm{C}+\mathrm{n}+\mathrm{n}\right)$ system, Ψ_1 may correspond to the interaction between the two neutrons, whereas Ψ_2 and Ψ_3 correspond to neutron-core interactions. Each component corresponds to a different Jacobi coordinate system (as illustrated in Fig. 1). The equation is given by:

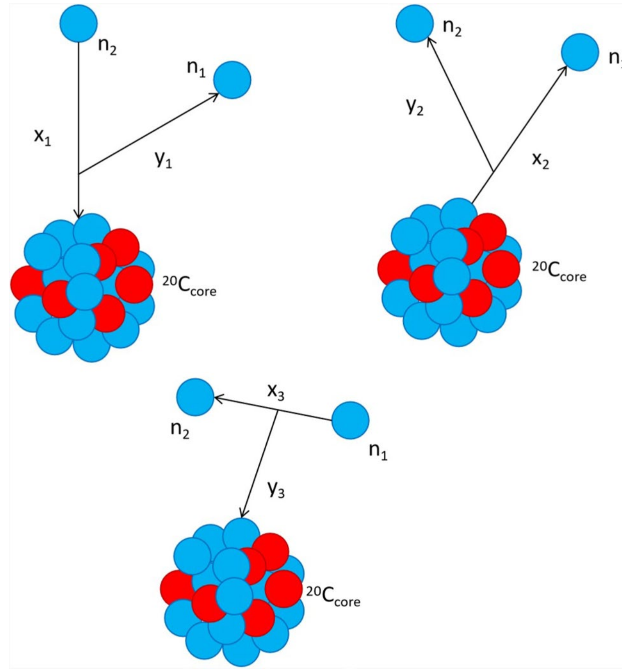

Fig. 1 (Color online) Three sets of Jacobi coordinates in the Faddeev formalism for $^{22}\mathrm{C}\left(^{20}\mathrm{C}+\mathrm{n}+\mathrm{n}\right)$ three-body system

$$\left(T_i + h + V_i - E\right)\psi_i^{JM} = -V_i\left(\psi_j^{JM} + \psi_k^{JM}\right). \tag{1}$$

The left-hand side represents the independent dynamics of the subsystem, including the kinetic energy T_i, core Hamiltonian $\hat{h}$, and two-body interaction potential V_i (encompassing both nuclear and Coulomb forces). The right-hand side represents how the superposition of the other two components feeds back into the evolution of the current component through the potential energy terms. This reflects the three-body coupling, the root cause of complexity in three-body problems.

Through this decomposition, the Faddeev equations transform the three-body problem into a coupled system of integro-differential equations, thereby avoiding the complexities of directly solving the high-dimensional Schrödinger equation. However, even with this simplified form, the numerical solution presents significant challenges owing to the multidimensional coordinate systems. To further reduce the computational dimensionality and achieve a unified description of the dynamic behavior across different Jacobi coordinates, the introduction of hyperspherical coordinates is essential.

By adopting the hyperspherical coordinate system, which includes the hyperradius ρ and hyperangles θ_i, the two-dimensional system of partial differential equations is transformed into a set of coupled, one-dimensional equations. The transformation of the Jacobi coordinates into hyperspherical coordinates takes the following form [36]:

$$\rho^2 = x_i^2 + y_i^2, \theta_i = \arctan\left(x_i/y_i\right). \tag{2}$$

The hyperradius ρ characterizes the global scale of the three-body system, being invariant under translational and rotational transformations as well as permutations of particle pairs (i, j), while correlating with the size of the nuclear core. In contrast, the hyperangle θ_i describes the relative configuration between the particles, which exhibits radial dependence and is correlated with the relative magnitudes of the two Jacobi coordinates. The wave function is expanded within the hyperspherical coordinates as [36, 37]

$$\begin{aligned}
&\psi_{\alpha_i}^{i,J}\left(x_i, y_i\right) = \rho^{-5/2} \sum_{K_i} \chi_{\alpha_i K_i}^{i,J}(\rho) \varphi_{K_i}^{l_{x_i} l_{y_i}}\left(\theta_i\right)\\
&\varphi_{K_i}^{l_{x_i} l_{y_i}}\left(\theta_i\right) = N_{K_i}^{l_{x_i} l_{y_i}} (\sin\theta)^{l_{x_i}} (\cos\theta)^{l_{y_i}} P_{n_i}^{l_{x_i}+1/2, l_{y_i}+1/2}\left(\cos 2\theta_i\right)\\
&\chi_{\alpha_i K_i}^{i,J}(\rho) = \textstyle\sum_0^{N_b} a_{K_i \alpha_i}^{in,J} R_n(\rho)\\
&R_n(\rho) \propto L_n^5(z) e^{-z/2}
\end{aligned} \tag{3}$$

φ_{k_i} denotes the hyperangular component, described by the Jacobi polynomial $P_{n_i}^{l_{x_i}+1/2, l_{y_i}+1/2}$; $\mathcal{N}_i$ is the normalization coefficient and K_i represents the hyperangular momentum directly related to the order of the corresponding Jacobi polynomial through $K_i = l_{x_i} + l_{y_i} + 2n_i\ (n_i = 0, 1, 2, \cdots)$. $\chi_{\alpha_i}^{K_i}$ represents the hyperradial component, which is expanded in terms of Laguerre polynomial basis functions.

Upon introducing the hyperspherical expansion into the Faddeev coupled equations, one obtains the following set of simultaneous linear equations:

$$\mathbf{H} a = E a. \tag{4}$$

Within the Faddeev equations, the matrix $\mathbf{H}$ requires several types of matrix elements:

$$\begin{aligned}
\hat{V}_{jk} = \hat{V}_i\left(x_i\right) =& V_i^{\mathrm{c}}\left(x_i\right) + \hat{SO} V_i^{\mathrm{so}}\left(x_i\right)\\
&+ \hat{Q} V_i^{\mathrm{Q}}\left(x_i\right) + \hat{T} V_i^{\mathrm{T}}\left(x_i\right) + \hat{SS} V_i^{\mathrm{SS}}\left(x_i\right)
\end{aligned} \tag{5}$$

$V_i^{\mathrm{c}}(x_i)$ denotes the central interaction. The spin-orbit (SO) coupling is described by the operator $\hat{SO}$ and radial form factor V_i^{so}. The tensor operator $\hat{Q}$ and radial form factor $V_i^{\mathrm{Q}}(x_i)$ account for the multipole-deformed potential. The standard tensor interaction is given by operator $\hat{T}$ with radial dependence $V_i^{\mathrm{T}}(x_i)$, whereas the spin-spin interaction is represented by $\hat{SS}$ and its form factor $V_i^{\mathrm{SS}}(x_i)$.

The central potential depends solely on the interparticle distance, with its operator form expressed as $V_i^{\mathrm{c}}(x_i)$ and is diagonal in the angular momentum and spin quantum numbers. Within a fixed Jacobi coordinate system, the matrix elements are given by

$$\begin{aligned}
\left\langle i : \alpha_i' \middle| V_i^{\mathrm{c}} \middle| i : \alpha_i \right\rangle =& \delta_{l'_{x_i} l_{x_i}} \delta_{l'_{y_i} l_{y_i}} \delta_{s'_{x_i} s_{x_i}} \delta_{J'_i J_i} \cdot\\
&\int V_i^{\mathrm{c}}\left(x_i\right) \varphi_{K_i'}^{l'_{x_i} l'_{y_i}}\left(\theta_i\right) \varphi_{K_i}^{l_{x_i} l_{y_i}}\left(\theta_i\right) \mathrm{d}\theta_i,
\end{aligned} \tag{6}$$

$\varphi_{K_i}^{l_{x_i} l_{y_i}}(\theta_i)$ represents the hyperspherical basis function. The spin-orbit potential takes the form $\hat{SO}\, V_i^{\mathrm{so}}(x_i) = \Gamma_{ij} \boldsymbol{l}_{x_i} \cdot \boldsymbol{s}_j + \Gamma_{ik} \boldsymbol{l}_{x_i} \cdot \boldsymbol{s}_k$, where its matrix elements incorporate scalar products of the orbital angular momentum with particle spins $\boldsymbol{s}_j$ or $\boldsymbol{s}_k$.

3 Numerical results and discussion

In this section, we perform detailed calculations of the ground-state properties of the ^{22}C nucleus using a three-body model based on the Faddeev equations. As a typical neutron-dripline nucleus, the experimentally deduced root-mean-square (r.m.s.) radius of ^{22}C, $r_{\mathrm{m}}^{\exp} = 3.296 \pm 0.123$ fm [33], serves as a key constraint in this study. Based on this, the parameters of the Woods-Saxon potential for the neutron-core interaction were determined using an inverse optimization approach.

In developing an interaction model ^{20}C + n, critical assumptions are implemented due to the absence of experimental data on core excitations: the ^{20}C core is treated as a rigid structure with spin-parity $J^\pi = 0^+$, enforcing Pauli blocking of the core orbitals $(1s_{1/2})^2$, $(1p_{3/2})^4$,$(1p_{1/2})^2$ and $(1d_{5/2})^6$ [38]; valence neutrons predominantly occupy the $(2s_{1/2})$ orbital with very weak binding [21].

The core-neutron interaction is described using a Woods-Saxon potential under the aforementioned assumptions, as shown in the following Eq. (7) [12, 37, 39], which takes the first two terms from Eq. (5).

$$V_{\text{n-core}}(r) = \frac{V_0}{1 + \exp\left(\frac{r - r_0}{a}\right)} + \frac{V_{\mathrm{so}}}{ra} \frac{\exp\left(\frac{r - r_0}{a}\right)}{\left[1 + \exp\left(\frac{r - r_0}{a}\right)\right]^2} \mathbf{L} \cdot \mathbf{S}, \tag{7}$$

The interaction potential parameters are determined by reproducing the experimentally deduced r.m.s. matter radii. Reference [33] reports the experimental r.m.s. matter radii of ^{22}C as $r_{\mathrm{m}}^{\exp} = 3.296 \pm 0.123$ fm. Achieving convergence within the experimental constraints necessitates reducing the radius parameter to $r_0 = 1.13 A^{1/3}$ fm (versus the conventional $1.25 A^{1/3}$ fm used in Ref. [12, 37]) – motivated by the monotonic increase of r.m.s. matter radii with r_0. When setting $r_0 = 1.13 A^{1/3}$ fm, the minimum achievable r.m.s.

Table 1 Input parameters for the ^{22}C three-body model and single-particle energies (units: MeV) lists the input values for three sets of parameters (1, 2, 3), represent the values adopted in calculations, while sets (4, 5) are used to analyze parameter selection criteria. All calculations employ Woods-Saxon potential depths $V_c^0 = -36.07$ MeV, $V_c^1 = -36.17$ MeV, with spin-orbit coupling strength $V_{so} = -45.51$ MeV

	$V_c^{l=2}$ (MeV)	r_0 (fm)	s_{3b}	r_{3b}	$1s_{1/2}$ (MeV)	$1p_{3/2}$ (MeV)	$1p_{1/2}$ (MeV)	$1d_{5/2}$ (MeV)	S_{2n} (MeV)	r_m^{cal}(fm)
1	−40.68	3.08	3	14	−18.306	−8.128	−1.698	−0.323	0.265	3.173
2	−38.31	3.2	3.5	14	−19.19	−9.188	−2.909	−0.56	0.656	3.296
3	−36.45	3.3	5	14	−19.889	−10.049	−3.961	−0.72	0.376	3.419
4	−38.21	3.2	3	14	−19.19	−9.188	−2.909	−0.521	1.02	3.296
5	−36.45	3.3	3	14	−19.889	−10.049	−3.961	−0.72	2.033	3.405

matter radii falls below the experimental lower limit, thereby encompassing the experimental range. The core-neutron potential strength $V_c^{l=2}$ is incrementally adjusted until r_m^{cal} precisely matches the experimental value of 3.173 fm. The maximum attainable r.m.s. matter radii through V_c^2 variation remains below the critical experimental values (3.296 fm and 3.419 fm). Consequently, a systematic adjustment of r_0 was implemented to translate the theoretical radius distribution, ensuring full coverage of the experimental value range. Specifically, distinct r_0 values are sequentially fixed to ensure that the adjustable range of the r.m.s. matter radii, achieved by tuning the neutron-core potential, encompasses each target experimental value.

From Table 1, it can be observed that r_m^{cal} also depends on the three-body interaction potential. Entries 2 and 4 demonstrate that identical r.m.s. matter radii values can correspond to multiple distinct sets of neutron-core and three-body interaction potentials. The analysis of entries 3 and 5 reveals that the neutron-core interaction potential plays a predominant role, whereas the three-body interaction potential also contributes significantly. The unique determination of this parameter set requires the incorporation of an additional constraint, namely, the two-neutron separation energy S_{2n}. A comparison of entries 3 and 5 reveals that within a constrained range of neutron-core potentials, S_{2n} exhibits a stronger correlation with the three-body interaction potential. Consequently, S_{2n} provides an approximate constraint for the three-body potential, enabling the subsequent precise calibration of V_c^2.

The two-neutron separation energy S_{2n}, obtained as an outcome of the calculation constrained by the matter radius, was then compared with theoretical and experimental values for validation. Reference [9] reports $S_{2n} = 0.56^{+0.27}_{-0.20}$ MeV, but calculations considering only two-body potentials exhibit significant deviations from this value. This discrepancy is mitigated by introducing a Gaussian-form three-body interaction in Eq. (8), which emulates the effects of core deformation or core excitation [35, 40, 41].

$$V_{3b}(\rho) = s_{3b} \exp\left[-\left(\frac{\rho}{r_{3b}}\right)^2\right]. \tag{8}$$

When identical three-body potential parameters $s_{3b} = 3$, $r_{3b} = 14$ are applied to parameter sets 1, 4, and 5, an inverse correlation is observed: stronger neutron-core interaction potentials V_c^2 yield larger two-neutron separation energies S_{2n}. These results exhibited significant deviations from the theoretical values. The deviation is reduced when the three-body potential strength is increased from the baseline of parameter set 5. This adjustment brings the calculated two-neutron separation energy S_{2n} into closer agreement with the theoretical value of $S_{2n} = 0.56^{+0.27}_{-0.20}$ MeV reported in Ref. [9]. The rationale for avoiding universally larger three-body potentials lies in set1's extremely shallow S_{2n} binding. Further enhancement induces a transition from the bound states to the continuum. Consequently, each parameter set requires a customized three-body potential strength.

At this stage, the input parameters, including two-body and three-body potentials have been calibrated by fixing the r.m.s. matter radii and benchmarking against the theoretical values of the two-neutron separation energy. These parameters are listed in Table 1, with sets 1, 2, and 3 selected as the primary configurations. Across these sets, only three parameters (V_c^2, s_{3b}, r_0) were varied, while all others remained fixed.

The hyperangular momentum cutoff $K_{max} = 20$ was employed throughout calculations to guarantee numerical convergence. The choice of K_{max} is briefly discussed in Ref. [42], larger values of K_{max} yield better convergence behavior and enable higher accuracy of the numerical solution. However, the influence of K_{max} on the results was significantly smaller than that of the two-body potential. Moreover, our study of the nucleus ^{22}C did not involve long-range interactions. Therefore, choosing $K_{max} = 20$ is adequate for the calculations.

The neutron-neutron interaction is described using the Gogny-Pires-Tourreil (GPT) potential [43], with the central, tensor, and spin-orbit terms included while omitting the spin-spin contribution. This potential provides good fits to the low-energy properties of nucleon-nucleon scattering.

Based on the parameter sets (sets 1, 2, and 3) listed in Table 1, the orbital energy levels, spatial configurations, and density distributions were systematically calculated. The bound states prohibited by the Pauli principle, such as the $1s_{1/2}$ and $1p_{3/2}$ orbitals, are eliminated through supersymmetric transformations, restricting the valence neutrons to the allowed $1d_{5/2}$ orbital. Furthermore, adjusting the s-wave and p-wave potential strengths along with the spin-orbit coupling strength revealed that the $(1s_{1/2})$, $(1p_{3/2})$, and $(1p_{1/2})$ states depend mainly on s-wave and p-wave contributions, which are not listed explicitly.

Table 1 lists the key single-particle orbital energies (units: MeV), where the orbital energy $1d_{5/2}$ ranges from -0.323 to -0.72 MeV, indicating that the orbital is in a weakly bound state. The deeply bound $1s_{1/2}$ orbital (-18.306 to -19.889 MeV) has a compact wave function and is Pauli-blocked for the valence neutrons. It should be noted that our research results do not rely on these energy values but rather on the single-particle wave functions. The different potential energies selected in this study produced almost identical single-particle wave functions for each occupied orbital, and all potential energy sets were configured such that the energy of the $2s_{1/2}$ single-particle state approached zero, consistent with the prescription in Ref. [12].

Because there is no centrifugal potential barrier for neutrons in the $2s_{1/2}$ orbital in the average potential field, the extremely weak neutron binding energy leads to significant tunneling effects. This significant tunneling implies the radial expansion of the wave function of the $s_{1/2}$ orbital. This energy level structure is consistent with the typical characteristics of the neutron drip-line nuclei. Additionally, owing to the expansion of the wave function, the dynamic coupling effects with other strongly bound orbitals are weakened beyond the static effects of the average potential field, indicating the presence of a pure $(s_{1/2})^2$ configuration and an unperturbed core. If there are two neutrons in the $2s_{1/2}$ orbital, their interaction is the only source of additional binding energy. Because the s-wave potential energy may be further weakened, the ground state energy of ^{22}C is considered to be the minimum value in this analysis.

We used the two- and three-body interaction models in Table 1 and solved the Faddeev equations to obtain the energy values and r.m.s. matter radii of the ground and excited states (relative to the ^{20}C + n threshold) of ^{22}C. The calculation results are presented in Table 2. All energy values are given relative to the ^{20}C + n + n threshold, and the values are similar.

$Z = 6$, $N = 14$ closed shell cores are referred to as closed cores. The neutron part of the ^{20}C ground state not only contains the $1d_{5/2}$ closed-shell configuration but also other configurations such as $2s_{1/2}$. In the ground state, the

Table 2 Energies and r.m.s. radii of the ground state and the excited state, calculated with three different three-body interaction parameter sets. Quantities with * correspond to the excited states. All energies are in units of MeV, while all lengths are in units of fm

	E (MeV)	r_{m} (fm)	E^* (MeV)	r^*_{m} (fm)
1	−0.265	3.173	2.442	3.561
2	−0.656	3.296	1.724	3.567
3	−0.376	3.419	1.902	3.579

two-neutron separation energy (S_{2n}) lies in the range of 0.265–0.656 MeV (equivalent to $-E$). The parameters were set based on the experimental values in Ref. [33], S_{2n} falls within the experimental range and is consistent with other theoretical values, $S_{2n} = 0.423 \pm 1.140$ MeV from Ref. [44] and $S_{2n} = -0.140 \pm 0.460$ MeV from Ref. [23] within the error range, confirming the reliability of the theoretical model.

In addition, the ^{22}C ground-state correlation core is introduced, featuring two valence neutrons occupying the halo s-orbital that must satisfy the orthogonality condition with the ^{20}C core s-orbital. The excited state has a spin-parity of $J^{\pi} = 0^{+}$. Notably, the excited state energy E is positive, indicating that the employed two-body and three-body potentials cannot bind the neutrons, which is consistent with the experimental phenomenon that there is no bound state in the ^{21}C nucleus [45].

To analyze the three-body configuration of ^{21}C, the average distance parameter of the valence neutrons was calculated (Table 3). In the ground state, the average distance between two neutrons is $r_{\mathrm{nn}} \approx 6.49$ fm, and the distance from the nucleus to the center of mass of the pair of neutrons is $r_{\mathrm{c,nn}} \approx 3.40$ fm. In the excited state, these values extend to $r_{\mathrm{nn}} \approx 8.90$ fm and $r_{\mathrm{c,nn}} \approx 4.65$ fm, which correspond to the size of a stable atomic nucleus with mass number $A \approx 60$. Therefore, the excited state of ^{22}C can be described as a giant halo state. The key finding was that the ratio remained constant.

$$\frac{r_{\mathrm{nn}}}{r_{\mathrm{c,nn}}} \approx \frac{r^*_{\mathrm{nn}}}{r^*_{\mathrm{c,nn}}} \approx 1.91 \tag{9}$$

The identical proportions obtained in both states indicate that these two states have similar geometric structures, with the main difference being the spatial discrete scaling factor.

In addition, the correlation density distribution between the ground and excited states of ^{22}C was analyzed. These values were calculated using the Jacobi coordinate system, with ^{20}C as the bystander particle. The formula for calculating the spatial correlation density distribution is as follows [41].

Table 3 Average distance r_{nn} between two valence neutrons in the ground state and excited state of ^{22}C, and average distance $r_{c,nn}$ from the core to the center of mass of the valence neutron pair. The superscript * denotes the excited state. All lengths are in units of fm

	r_{nn} (fm)	$r_{c,nn}$ (fm)	r^*_{nn} (fm)	$r^*_{c,nn}$ (fm)
1	6.492	3.404	9.577	5.004
2	6.823	3.578	8.896	4.653
3	6.989	3.665	8.693	4.548

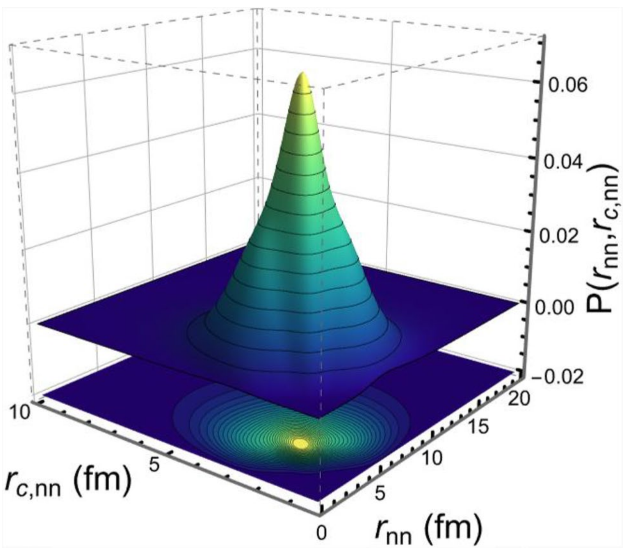

Fig. 2 (Color online) Spatial distribution of two valence neutrons in the ground state

$$P\left(r_{nn}, r_{c,nn}\right) \equiv x^2y^2 \int \left|\Psi_i^{JM}(x,y)\right|^2 d\Omega_{x_i} d\Omega_{y_i} \tag{10}$$

The spatial distributions of the two valence neutrons in the ground and excited states are shown in Figs. 2 and 3, respectively. The spatial distribution function peaks at $(r_{nn}, r_{c,nn}) \approx (6.5, 3.5)$ fm (Fig. 2) in the ground state, corresponding to the maximum probability density. This configuration is consistent with a compact three-body configuration, whereas the main peak of the maximum probability density for the excited state is at $(9.5, 4.5)$ fm, with a secondary peak at $(12, 5.5)$ fm, which originates from the contribution of the $(1d)^2$ orbital (Fig. 3). This double-peak structure reflects the orbital rearrangement effect in the excited state: some neutrons transition from the s-wave to the d-wave, causing the spatial configuration to differentiate into two modes: compact and extended.

Orbital occupancy analysis reveals the s-wave dominant characteristics of ^{22}C. In the ground state, $(2s_{1/2})^2$ accounts for 97.77%, whereas the d-wave component

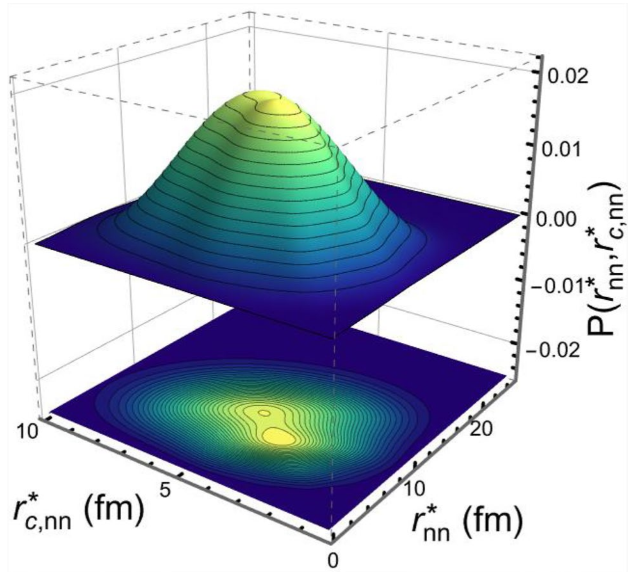

Fig. 3 (Color online) Spatial distribution of two valence neutrons in the excited state

accounts for only 2.23%; in the excited state, $(2s_{1/2})^2$ decreases to 72.90%, whereas $(1d_{5/2})^2$ increases to 27.10%. This change coincides with the secondary peak position of the density distribution, indicating the existence of s-d orbital mixing in the excited state. This may be because the d-wave component acquires significant weight and core polarization, and the extended halo structure enhances the coupling between the core and valence neutrons, inducing orbital mixing. It is worth noting that despite the increase in d-wave components, s-waves still dominate (> 70%); thus, the excited state is essentially the same as the ground state, with an s-wave halo nucleus [12], but exhibiting more complex multi-orbit coupling effects.

The Efimov effect is a universal quantum phenomenon in three-body systems, in which an effective long-range attraction emerges from short-range two-body interactions near resonance, leading to a series of weakly bound states exhibiting discrete scale invariance [46]. Given the significantly larger r.m.s. radii and more diffuse spatial distribution of the excited state, it can be characterized as an Efimov state in the halo nucleus [47, 48]. Since ^{22}C has been confirmed to be a double-neutron halo nucleus, Ref. [49] pointed out that the Efimov effect is most likely to be observed in double neutron halo nuclei. The study also revealed an interesting geometric similarity between the ground and excited state configurations—in Efimov physics, two consecutive Efimov states can be related through discrete spatial scaling factors [50]. The identical ratio relationship between r_{nn} and $r_{c,nn}$ in the ground and excited states of ^{22}C [Eq. (9)] indicates that the nuclear configurations of the two states have highly similar geometric shapes, indicating that discrete scaling symmetry exists. The features we discovered in ^{22}C are highly consistent with the theoretical explanation of the Efimov states [51].

4 Conclusion

In this study, we systematically investigated the structural properties of the neutron-rich nucleus ^{22}C using a three-body Faddeev approach constrained by the experimentally determined matter radius. Our calculations employed the Woods-Saxon potential for the neutron-core interaction and introduced a Gaussian-form three-body potential to account for core deformation effects. By fine-tuning the potential parameters, the experimental matter radius ($r_{\rm m} = 3.296 \pm 0.123\,\text{fm}$) was successfully reproduced, while the derived two-neutron separation energy S_{2n} was in agreement with both theoretical and experimental values, confirming the weakly bound nature of ^{22}C.

The ground state of ^{22}C exhibits a dominant $(2s_{1/2})^2$ configuration with a weakly bound $1d_{5/2}$ orbital, corresponding to a two-neutron separation energy (S_{2n}) in the range of 0.265–0.656 MeV, consistent with previous results. The excited state displays an extended s-d hybrid structure (s-wave $> 70\%$) and a double-peak spatial distribution. The constant ratio $r_{\rm nn}/r_{\rm c,nn} \approx 1.91$ between states suggests a discrete scaling symmetry, supporting ^{22}C as an Efimov candidate in Borromean nuclei.

Our results highlight the interplay between the neutron and core interaction and three-body forces in shaping the properties of ^{22}C. The consistency between our predictions and experimental data validates the three-body approach as a powerful tool for studying neutron-rich nuclei. Future work could explore the dynamical effects of core excitation and the role of higher-order interactions in refining the description of ^{22}C and similar dripline nuclei. These insights contribute to a deeper understanding of exotic nuclear structures and their connections to universal few-body phenomena.

Author Contributions All authors contributed to the study conception and design. Material preparation, data collection and analysis were performed by Yi-Le Fan, Qing-Rui Sun and Cheng-Jun Feng. The first draft of the manuscript was written by Yi-Le Fan and all authors commented on previous versions of the manuscript. All authors read and approved the final manuscript.

Data Availability The data that support the findings of this study are openly available in Science Data Bank at https://cstr.cn/31253.11.sciencedb.j00186.00890 and https://www.doi.org/10.57760/sciencedb.j00186.00890.

Declarations

Conflict of interest The authors declare that they have no conflict of interest.

References

1. F.G. Kondev, M. Wang, W.J. Huang et al., The NUBASE2020 evaluation of nuclear physics properties. Chin. Phys. C **45**, 030001 (2021). https://doi.org/10.1088/1674-1137/abddae
2. M. Wang, W.J. Huang, F.G. Kondev et al., The AME 2020 atomic mass evaluation (II). Tables, graphs and references. Chin. Phys. C. **45**, 030003(2021). https://doi.org/10.1088/1674-1137/abddaf
3. S.A. Giuliani, Z. Matheson, W. Nazarewicz et al., Colloquium: Superheavy elements: oganesson and beyond. Rev. Mod. Phys. **91**, 011001 (2019). https://doi.org/10.1103/RevModPhys.91.011001
4. D.S. Ahn, N. Fukuda, H. Geissel et al., Location of the neutron dripline at fluorine and neon. Phys. Rev. Lett. **123**, 212501 (2019). https://doi.org/10.1103/PhysRevLett.123.212501
5. D.S. Ahn, J. Amano, H. Baba et al., Discovery of ^{39}Na. Phys. Rev. Lett. **129**, 212502 (2022). https://doi.org/10.1103/PhysRevLett.129.212502
6. H.L. Crawford, V. Tripathi, J.M. Allmond et al., Crossing $N = 28$ toward the neutron drip line: first measurement of half-lives at FRIB. Phys. Rev. Lett. **129**, 212501 (2022). https://doi.org/10.1103/PhysRevLett.129.212501
7. K.Y. Zhang, S.Q. Zhang, J. Meng, Possible neutron halo in the triaxial nucleus ^{42}Al. Phys. Rev. C **108**, L041301 (2023). https://doi.org/10.1103/PhysRevC.108.L041301
8. T. Nagahisa, W. Horiuchi, Examination of the ^{22}C radius determination with interaction cross sections. Phys. Rev. C **97**, 054614 (2018). https://doi.org/10.1103/PhysRevC.97.054614
9. Y. Togano, T. Nakamura, Y. Kondo et al., Interaction cross section study of the two-neutron halo nucleus ^{22}C. Phys. Lett. B **761**, 412–418 (2016). https://doi.org/10.1016/j.physletb.2016.08.062
10. B. Acharya, C. Ji, D.R. Phillips, Implications of a matter-radius measurement for the structure of Carbon-22. Phys. Lett. B **723**, 196–200 (2013). https://doi.org/10.1016/j.physletb.2013.04.055
11. P. Naidon, S. Endo, Efimov physics: a review. Rep. Prog. Phys. **80**, 056001 (2017). https://doi.org/10.1088/1361-6633/aa50e8
12. W. Horiuchi, Y. Suzuki, ^{22}C: An S-wave two-neutron halo nucleus. Phys. Rev. C **74**, 034311 (2006). https://doi.org/10.1103/PhysRevC.74.034311
13. W. Horiuchi, Y. Suzuki, B. Abu-Ibrahim et al., Systematic analysis of reaction cross sections of carbon isotopes. Phys. Rev. C **75**, 044607 (2007). https://doi.org/10.1103/PhysRevC.75.044607
14. K. Tanaka, T. Yamaguchi, T. Suzuki et al., Observation of a large reaction cross section in the drip-line nucleus ^{22}C. Phys. Rev. Lett. **104**, 062701 (2010). https://doi.org/10.1103/PhysRevLett.104.062701
15. O. Sorlin, M.G. Porquet, Nuclear magic numbers: new features far from stability. Prog. Part. Nucl. Phys. **61**, 602–673 (2008). https://doi.org/10.1016/j.ppnp.2008.05.001
16. D.T. Tran, H.J. Ong, G. Hagen et al., Evidence for prevalent $Z = 6$ magic number in neutron-rich carbon isotopes. Nat. Commun. **9**, 1594 (2018). https://doi.org/10.1038/s41467-018-04024-y
17. T. Otsuka, A. Gade, O. Sorlin et al., Evolution of shell structure in exotic nuclei. Rev. Mod. Phys. **92**, 015002 (2020). https://doi.org/10.1103/RevModPhys.92.015002
18. X.-X. Sun, J. Zhao, S.-G. Zhou, Shrunk halo and quenched shell gap at $N = 16$ in ^{22}C: inversion of sd states and deformation

effects. Phys. Lett. B **785**, 530–535 (2018). https://doi.org/10.1016/j.physletb.2018.08.071
19. X.-X. Sun, J. Zhao, S.-G. Zhou, Study of ground state properties of carbon isotopes with deformed relativistic Hartree-Bogoliubov theory in continuum. Nucl. Phys. A **1003**, 122011 (2020). https://doi.org/10.1016/j.nuclphysa.2020.122011
20. X.-X. Sun, S.-G. Zhou, Rotating deformed halo nuclei and shape decoupling effects. Sci. Bull. **66**, 2072–2078 (2021). https://doi.org/10.1016/j.scib.2021.07.005
21. N. Kobayashi, T. Nakamura, J.A. Tostevin et al., One- and two-neutron removal reactions from the most neutron-rich carbon isotopes. Phys. Rev. C **86**, 054604 (2012). https://doi.org/10.1103/PhysRevC.86.054604
22. S. Mosby, N.S. Badger, T. Baumann et al., Search for ^{21}C and constraints on ^{22}C. Nucl. Phys. A **909**, 69–78 (2013). https://doi.org/10.1016/j.nuclphysa.2013.04.004
23. L. Gaudefroy, W. Mittig, N.A. Orr et al., Direct mass measurements of ^{19}B, ^{22}C, ^{29}F, ^{31}Ne, ^{34}Na and Other Light Exotic Nuclei. Phys. Rev. Lett. **109**, 202503 (2012). https://doi.org/10.1103/PhysRevLett.109.202503
24. H.T. Fortune, R. Sherr, Binding energy of ^{22}C. Phys. Rev. C **85**, 027303 (2012). https://doi.org/10.1103/PhysRevC.85.027303
25. L. Coraggio, A. Covello, A. Gargano et al., Shell-model calculations for neutron-rich carbon isotopes with a chiral nucleon-nucleon potential. Phys. Rev. C **81**, 064303 (2010). https://doi.org/10.1103/PhysRevC.81.064303
26. N.B. Shulgina, S.N. Ershov, J.S. Vaagen et al., Superhalo of ^{22}C reexamined. Phys. Rev. C **97**, 064307 (2018). https://doi.org/10.1103/PhysRevC.97.064307
27. P. Choudhary, P.C. Srivastava, M. Gennari et al., Ab initio no-core shell-model description of $^{10-14}$C isotopes. Phys. Rev. C **107**, 014309 (2023). https://doi.org/10.1103/PhysRevC.107.014309
28. B.S. Hu, Q. Wu, Z.H. Sun et al., Ab initio Gamow in-medium similarity renormalization group with resonance and continuum. Phys. Rev. C **99**, 061302 (2019). https://doi.org/10.1103/PhysRevC.99.061302
29. X.-Y. Xu, S.-Q. Fan, Q. Yuan et al., Progress in ab initio in-medium similarity renormalization group and coupled-channel method with coupling to the continuum. Nucl. Sci. Tech. **35**, 215 (2024). https://doi.org/10.1007/s41365-024-01585-0
30. H.T. Fortune, Update on matter radii of carbon nuclei. Phys. Rev. C **94**, 064307 (2016). https://doi.org/10.1103/PhysRevC.94.064307
31. S.N. Ershov, J.S. Vaagen, M.V. Zhukov, Binding energy constraint on matter radius and soft dipole excitations of ^{22}C. Phys. Rev. C **86**, 034331 (2012). https://doi.org/10.1103/PhysRevC.86.034331
32. R. Sherr, Simple model of neutron halo nuclei. Phys. Rev. C **54**, 1177–1181 (1996). https://doi.org/10.1103/PhysRevC.54.1177
33. M. Mouadil, A. Khouaja, O. Jdair et al., Matter distribution of $^{12-20,22}$C isotopes. Phys. Rev. C **109**, 054330 (2024). https://doi.org/10.1103/PhysRevC.109.054330
34. R. Kanungo, W. Horiuchi, G. Hagen et al., Proton distribution radii of $^{12-19}$C illuminate features of neutron halos. Phys. Rev. Lett. **117**, 102501 (2016). https://doi.org/10.1103/PhysRevLett.117.102501
35. I.J. Thompson, F.M. Nunes, B.V. Danilin, FaCE: a tool for three body Faddeev calculations with core excitation. Comput. Phys. Commun. **161**, 87–107 (2004). https://doi.org/10.1016/j.cpc.2004.03.007
36. F.M. Nunes, J.A. Christley, I.J. Thompson et al., Core excitation in three-body systems: application to ^{12}Be. Nucl. Phys. A **609**, 43–73 (1996). https://doi.org/10.1016/0375-9474(96)00284-9
37. Y.Y. Chu, Z.Z. Ren, C. Xu, Properties of proton-rich nuclei in a three-body model. Eur. Phys. J. A **37**, 361–366 (2008). https://doi.org/10.1140/epja/i2008-10626-2
38. I.J. Thompson, B.V. Danilin, V.D. Efros et al., Pauli blocking in three-body models of halo nuclei. Phys. Rev. C **61**, 024318 (2000). https://doi.org/10.1103/PhysRevC.61.024318
39. S. Chen, Y.Y. Chu, Z.Z. Ren, Density-dependent potential for multi-neutron halo nuclei. Chin. Phys. C **33**, 639 (2009). https://doi.org/10.1088/1674-1137/33/8/008
40. A. Kievsky, E. Garrido, C. Romero-Redondo et al., The helium trimer with soft-core potentials. Few-Body Syst. **51**, 259–269 (2011). https://doi.org/10.1007/s00601-011-0226-9
41. C. Romero-Redondo, E. Garrido, D.V. Fedorov et al., Three-body structure of low-lying ^{12}Be states. Phys. Rev. C **77**, 054313 (2008). https://doi.org/10.1103/PhysRevC.77.054313
42. D. Bai, Z.Z. Ren, T.K. Dong, Two-neutron halo state of ^{15}B around 3.48 MeV by a three-body model. Chin. Phys. C. **42**, 064103 (2018). https://doi.org/10.1088/1674-1137/42/6/064103
43. D. Gogny, P. Pires, R. De Tourreil, A smooth realistic local nucleon-nucleon force suitable for nuclear Hartree-Fock calculations. Phys. Lett. B **32**, 591–595 (1970). https://doi.org/10.1016/0370-2693(70)90552-6
44. G. Audi, A.H. Wapstra, C. Thibault, The Ame 2003 atomic mass evaluation: (II). Tables, graphs and references. Nucl. Phys. A. **729**, 337–676 (2003). https://doi.org/10.1016/j.nuclphysa.2003.11.003
45. T. Suzuki, T. Otsuka, C.X. Yuan et al., Two-neutron halo from the low-energy limit of neutron-neutron interaction: Applications to drip-line nuclei ^{22}C and ^{24}O. Phys. Lett. B **753**, 199–203 (2016). https://doi.org/10.1016/j.physletb.2015.12.001
46. S. Endo, E. Epelbaum, P. Naidon et al., Three-body forces and Efimov physics in nuclei and atoms. Eur. Phys. J. A **61**, 9 (2025). https://doi.org/10.1140/epja/s10050-024-01467-4
47. Z.Z. Ren, Weakly bound states of a three-body system. Phys. Rev. C **49**, 1281–1284 (1994). https://doi.org/10.1103/PhysRevC.49.1281
48. Q.H. Lin, Z.Z. Ren, Efimov effect in a three-body system with attractive r^{-2} two-body interactions. J. Phys. G Nucl. Part. Phys. **39**, 035102 (2012). https://doi.org/10.1088/0954-3899/39/3/035102
49. D.V. Fedorov, A.S. Jensen, K. Riisager, Efimov states in halo nuclei. Phys. Rev. Lett. **73**, 2817–2820 (1994). https://doi.org/10.1103/PhysRevLett.73.2817
50. E. Nielsen, D.V. Fedorov, A.S. Jensen, The structure of the atomic helium trimers: halos and Efimov states. J. Phys. B At. Mol. Opt. Phys. **31**, 4085 (1998). https://doi.org/10.1088/0953-4075/31/18/008
51. E. Braaten, H.-W. Hammer, Universality in few-body systems with large scattering length. Phys. Rep. **428**, 259–390 (2006). https://doi.org/10.1016/j.physrep.2006.03.001